mater.scichina.com link.springer.com https://doi.org/10.1007/s40843-025-4034-3

Active site concentration steers the reaction pathway of CO_2 electroreduction

Xiaoyue Zhu[1†], Zijian Li[3†], Yuhang Zhang[1], Yanru Geng[1], Min Gyu Kim[4], Haeseong Jang[2*], Shangguo Liu[1*], Xien Liu[1*] and Qing Qin[1*]

ABSTRACT Critical influence of local active-site concentration and configuration on CO_2 reduction selectivity remains rarely explored, due to the challenge in constructing well-defined structures. In this study, we employ a molten salt-assisted strategy to synthesize Ce-O_V-Cu cascade catalyst with tunable configurations and relative concentrations of Cu and Ce-O_V sites. Two distinct geometries were constructed: one featuring dense Cu sites surrounding Ce-O_V, and another with isolated Cu centers encapsulated by Ce-O_V. These configurations effectively direct the key *CHO or *COH intermediates toward either coupling with *CO or hydrogenation with *H, thereby switching product selectivity. The $CuCe_{10}O_x$ catalyst with isolated copper centers achieves a high CH_4 Faradaic efficiency (FE) of 61.7% at −1.6 V vs. reversible hydrogen electrode (RHE), whereas the local Cu-rich $Cu_{10}CeO_x$ variant favors C_2 production with a maximum FE of 61.5% at −1.4 V vs. RHE. Mechanistic studies reveal that locally concentrated Cu sites exhibit strong *CO_2 binding affinity, enhancing *CO surface coverage and facilitating *CO–*COH coupling; while Ce-O_V-rich regions with isolated copper center supply abundant availability *H, promoting deep protonation of *CHO intermediate toward CH_4. This work offers valuable insights into catalyst design, where manipulating structural chemistry guides catalytic processes toward targeted CO_2RR products.

Keywords: electrocatalyst, CO_2 reduction reaction, active site concentration, reaction pathway, selectivity

INTRODUCTION

As global energy demand grows exponentially, the resulting massive CO_2 emissions pose a serious threat to the environment [1]. Current research efforts are focused on carbon capture and storage (CCS) and CO_2 resource utilization technologies. Among these, carbon dioxide reduction reaction (CO_2RR) is regarded as a strategic approach to achieving a closed artificial carbon cycle. This technology enables the conversion of intermittent electricity from renewable energy sources (such as solar and wind power) into high-value hydrocarbon fuels and syngas, thereby facilitating chemical energy storage [2–5]. However, the CO_2RR involves multi-electron transfer processes and a complex reaction network, making precise control over reaction pathways and selective conversion of key intermediates a central scientific challenge in the field [6,7].

The limited product selectivity in the CO_2RR primarily arises from the competition among multiple possible reaction pathways [8]. Therefore, the key issue lies in steering the reaction toward desired products. In this context, the local concentration and configuration of active sites play a critical role in mediating the catalytic pathway. As reported by Zhai and coworkers [9], a high density of active sites can lead to the aggregation of gas molecules from adjacent sites. Alternatively, an appropriate concentration of active sites can enhance the reaction rate and increase the probability of intermediates encountering one another. Moreover, in catalysts with multiple active sites, a high local density of homologous active sites can raise the local coverage of homologous intermediates, promote collision and reaction probabilities, and lower the reaction energy barrier [10]. In the case of CO_2RR over Cu-based catalysts—the only type capable of driving C–C coupling—a variety of intermediates are involved in the electrochemical process. Among these, species such as *CO or *CHO play a decisive role in determining the subsequent pathway and product selectivity [11,12]. For example, directing the reaction toward C–C coupling versus deep hydrogenation can selectively yield C_2 products or CH_4 [13]. In Cu single-atom and low-copper-content catalyst systems, isolated and well-dispersed copper active sites lead to a low and sparse coverage of *CO intermediates. This distribution characteristic of adsorbates favors the formation of C_1 products [14]. In contrast, a higher density of active sites would promote the generation of C_2 products. However, precisely controlling the local concentration of active sites to steer reaction pathways and product distributions remains challenging, primarily due to the difficulty in fabricating catalysts with well-controlled active site density.

CuCe composite catalysts have emerged as a research focus in the field of electrocatalysis due to their unique advantages in regulating the product selectivity and catalytic stability of CO_2RR [15]. However, current research predominantly focuses on the influence of parameters such as the overall composition

[1] State Key Laboratory of Advanced Optical Polymer and Manufacturing Technology, College of Chemical Engineering, Qingdao University of Science and Technology, Qingdao 266042, China
[2] Department of Intelligence Energy and Industry, Chung-Ang University, Seoul 06974, Republic of Korea
[3] Department of Chemistry, City University of Hong Kong, Hong Kong SAR 999077, China
[4] Beamline Research Division, Pohang Accelerator Laboratory (PAL), Pohang 37673, Republic of Korea
† Equally contributed to this work.
* Corresponding author (email: hjang4765@gmail.com; liusg@qust.edu.cn; liuxien@qust.edu.cn; qinqing@qust.edu.cn)

© The Author(s) 2026. This article is published with open access at link.springer.com.

ratio and macroscopic morphology of catalysts on catalytic performance, with gaps remaining in the precise regulation of local copper active sites and the elucidation of their underlying mechanisms. On one hand, existing CuCe systems predominantly feature heterogeneous mixed structures, making it challenging to effectively isolate the coupled effects of copper site concentration, interfacial interactions, and Ce-based carrier crystal phases; On the other hand, the absence of structurally defined model catalysts as research platforms prevents the systematic separation and verification of intrinsic correlations between local copper site concentrations and the overall geometric configuration of the catalyst. In light of this, we developed a molten salt-assisted approach for the controlled synthesis of Cu-O_V-Ce cascade catalysts with tunable local microstructures. Using these model systems, we systematically investigated the influence of local active site configuration and concentration on the reaction pathways of CO_2 reduction. The $CuCe_{10}O_x$ catalyst, characterized by isolated copper centers surrounded by Ce-O_V sites, achieved a notable Faradaic efficiency (FE) of 61.7% for CH_4 at −1.6 V versus reversible hydrogen electrode (RHE). In contrast, $Cu_{10}CeO_x$, which features localized Cu aggregation regions, exhibited enhanced C_2 production with a maximum FE of 61.5% at −1.4 V versus RHE. The catalytic mechanism was elucidated through advanced characterization techniques, including X-ray absorption near-edge structure (XANES), extended X-ray absorption fine structure (EXAFS), *in situ* Fourier transform infrared (FTIR) and Raman spectroscopy, combined with detailed electrochemical analysis and density functional theory (DFT) calculation. These findings contribute to the identification of optimal catalyst configurations for selective CH_4 and C_2 production, offering valuable guidance for the rational design of efficient catalysts in energy conversion technologies.

EXPERIMENTAL SECTION

Chemicals

$Cu(NO_3)_2{\cdot}3H_2O$ (*M*: 241.6, ⩾98%) and $Ce(NO_3)_4{\cdot}6H_2O$ (*M*: 456.9, 99.9%) were purchased from Macklin. $NaNO_3$ (*M*: 84.99, 99%) was purchased from Huaxia Reagent Company. All reagents were used without further purification.

Synthesis of the $Cu_zCe_yO_x$ catalyst

The synthesis of $Cu_zCe_yO_x$ was via a molten salt-assisted synthetic method. First, 5 g of $NaNO_3$ was added to a crucible and then put in a muffle furnace. After heating to 350 °C for 20 min, the $NaNO_3$ was molten. $Cu(NO_3)_2{\cdot}3H_2O$ (0.2 g) and $Ce(NO_3)_4{\cdot}6H_2O$(0.036 g) (molar ratio of Cu to Ce is 10:1) were added to the crucible. After 3 min, the crucible was removed from the muffle furnace and cooled to room temperature naturally. The product was washed several times with deionized water to remove $NaNO_3$. Finally, the product was redispersed in ultrapure water and freeze-dried. The collected products were named $Cu_{10}CeO_x$. While the $Cu_zCe_yO_x$ catalysts were synthesized with varied molar ratio of Cu to Ce.

Synthesis of CuO and CeO_2 catalysts

CeO_2 was synthesized following the same procedure as that used for the CuCe catalysts, but without the addition of $Cu(NO_3)_2{\cdot}3H_2O$. Similarly, the CuO catalyst was prepared using the same method in the absence of $Ce(NO_3)_4{\cdot}6H_2O$.

RESULTS AND DISCUSSION

Catalyst synthesis and characterization

As illustrated in Fig. 1a, Cu–Ce-based heterojunction catalysts and solid solution catalysts were fabricated via the molten salt method using $NaNO_3$ as the solvent. For clarity, the samples were designated based on the feeding ratios: for instance, $CuCe_{10}O_x$ (Cu:Ce = 1:10) and $Cu_{10}CeO_x$ (Cu:Ce = 10:1), among others. Scanning electron microscopy (SEM) characterization reveals that pure CuO consists of elongated nanoclusters (Fig. S1a), whereas pure CeO_2 is composed of irregular polyhedral nanoparticles (Fig. S1b). Particle size analysis indicates that the diameters of pure CeO_2 nanoparticles range from approximately 150 to 300 nm. In contrast, the $Cu_{10}CeO_x$ catalyst exhibits a heterojunction structure, with CeO_2 nanoparticles supported on CuO nanoclusters (Fig. S1c). As for the $CuCe_{10}O_x$ catalyst (Fig. S1d), it also displays a nanoparticle-based morphology; however, compared with pure CeO_2, its particle size increases, with diameters ranging from approximately 200 to 500 nm. High-resolution transmission electron microscopy (HRTEM) image in Fig. 1b, along with the corresponding fast Fourier transform (FFT) pattern shown in the inset, reveals the microstructure of the $CuCe_{10}O_x$ catalyst. The material exhibits a cubic phase structure, with a measured lattice spacing of 3.24 Å, which can be indexed to the (111) plane of cubic CeO_2. For comparison, Fig. 1c and Fig. S2 display the HRTEM image of pristine CeO_2, showing a lattice spacing of 3.15 Å for the same (111) plane. This corresponds to a lattice expansion of approximately 2.9% in $CuCe_{10}O_x$ relative to pure CeO_2 (Fig. 1h), a phenomenon attributed to the incorporation of a small amount of Cu atoms into the CeO_2 lattice, resulting in the formation of a solid solution. In this structure, the Cu sites are present at low concentrations and are highly dispersed, leading to a low concentration of *CO intermediates. As a result, effective C–C coupling reactions are hindered [16].

Moreover, the abundant CeO_2 substrate supplies ample *H intermediates, promoting the protonation of *CO (e.g., *CO + *H → *CHO or similar pathways), which favors the formation of C_1 products such as CH_4. As shown in Fig. 1d, the $Cu_{10}CeO_x$ catalyst exhibits a typical heterojunction structure with a distinct interface, as marked by the red line. The measured lattice spacing of 2.75 Å corresponds to the (110) plane of CuO (Fig. 1e), while the spacing of 3.12 Å is attributed to the (111) plane of CeO_2 (Fig. 1f).

Fig. 1g displays the X-ray diffraction (XRD) patterns of the representative as-prepared Cu–Ce catalysts, further confirming the composition and structure of $CuCe_{10}O_x$ and $Cu_{10}CeO_x$. As shown, only the diffraction peaks corresponding to CeO_2 (PDF#81-0792) are observed in the pattern of $CuCe_{10}O_x$, indicating the formation of a solid solution where Cu is incorporated into the CeO_2 lattice. In contrast, the XRD pattern of $Cu_{10}CeO_x$ reveals the presence of two distinct phases: CuO (PDF#80-1917) and CeO_2. These results are consistent with the HRTEM analysis. Existing studies have indicated that the (110) crystal plane of Cu exhibits specific adsorption characteristics toward the *CO intermediate, thereby facilitating the C–C coupling reaction. Furthermore, constructing a bimetallic heterojunction structure can effectively modulate the binding energy of key intermediates, overcoming the limitations imposed by linear scaling relations. The interfacial charge redistribution induced by such a structure significantly reduces the energy barrier of

© The Author(s) 2026. This article is published with open access at link.springer.com.

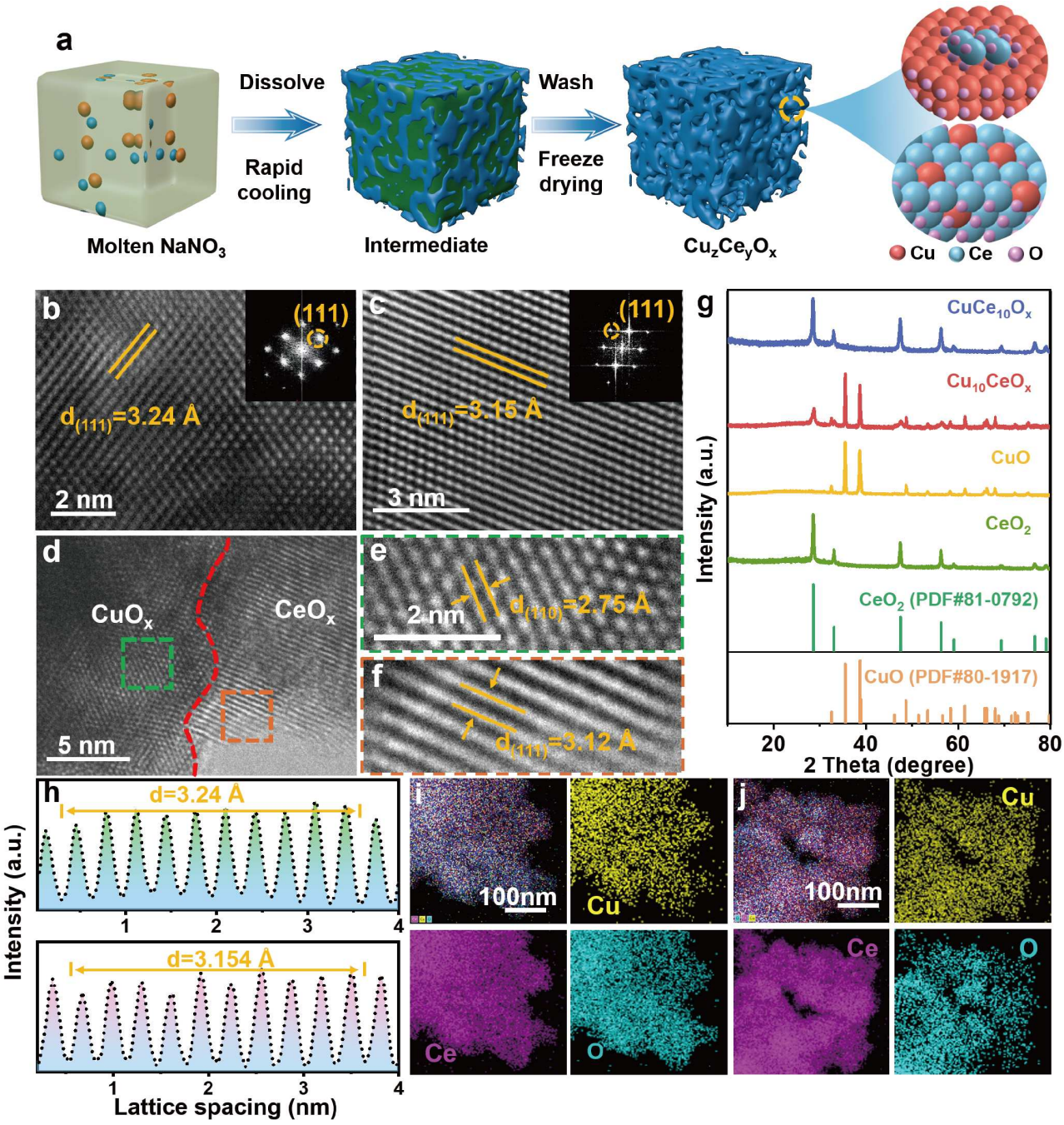


Figure 1 Synthesis and characterizations of $Cu_zCe_yO_x$ catalysts. (a) Schematic illustration of the synthetic procedure. HRTEM images of (b) $CuCe_{10}O_x$ (inset: FFT pattern), (c) CeO_2 (inset: FFT pattern), and (d) $Cu_{10}CeO_x$. (e) Lattice spacing corresponding to the green dotted areas in (d). (f) Lattice spacing corresponding to the orange dotted areas in (d). (g) XRD patterns of $Cu_{10}CeO_x$, $CuCe_{10}O_x$, CeO_2 and CuO. (h) Intensity line profiles of $CuCe_{10}O_x$ (top) and CeO_2 (bottom). (i) High-angle annular dark field scanning transmission electron microscopy (HAADF-STEM) image of $CuCe_{10}O_x$ and corresponding elemental mappings of O, Ce, and Cu. (j) HAADF-STEM image of $Cu_{10}CeO_x$ and corresponding elemental mappings of O, Ce, and Cu.

critical steps (e.g., *CO → *COH), ultimately promoting the formation of multi-carbon products such as ethanol and ethylene [17–19]. It is noteworthy that an excessive accumulation of *H intermediates could markedly enhance the hydrogen evolution reaction (HER). Therefore, tuning the Ce-to-Cu ratio is essential to maintain an appropriate balance between *H and *CO intermediate coverage, thereby optimizing the selectivity toward target products. The elemental distribution in the catalysts was further examined through elemental mapping and energy-dispersive spectroscopy (EDS), as shown in Fig. 1i, j and Figs S3–S6. The results indicate that in both $CuCe_{10}O_x$ and $Cu_{10}CeO_x$ catalysts, the elements Cu, Ce, and O are uniformly distributed, with no noticeable elemental enrichment or phase separation, confirming the high structural homogeneity of the synthesized samples.

Fig. 2a presents the XRD patterns of catalysts with varying Cu/Ce molar ratios. The analysis reveals that pristine CuO exhibits characteristic diffraction peaks corresponding to the monoclinic

© The Author(s) 2026. This article is published with open access at link.springer.com.

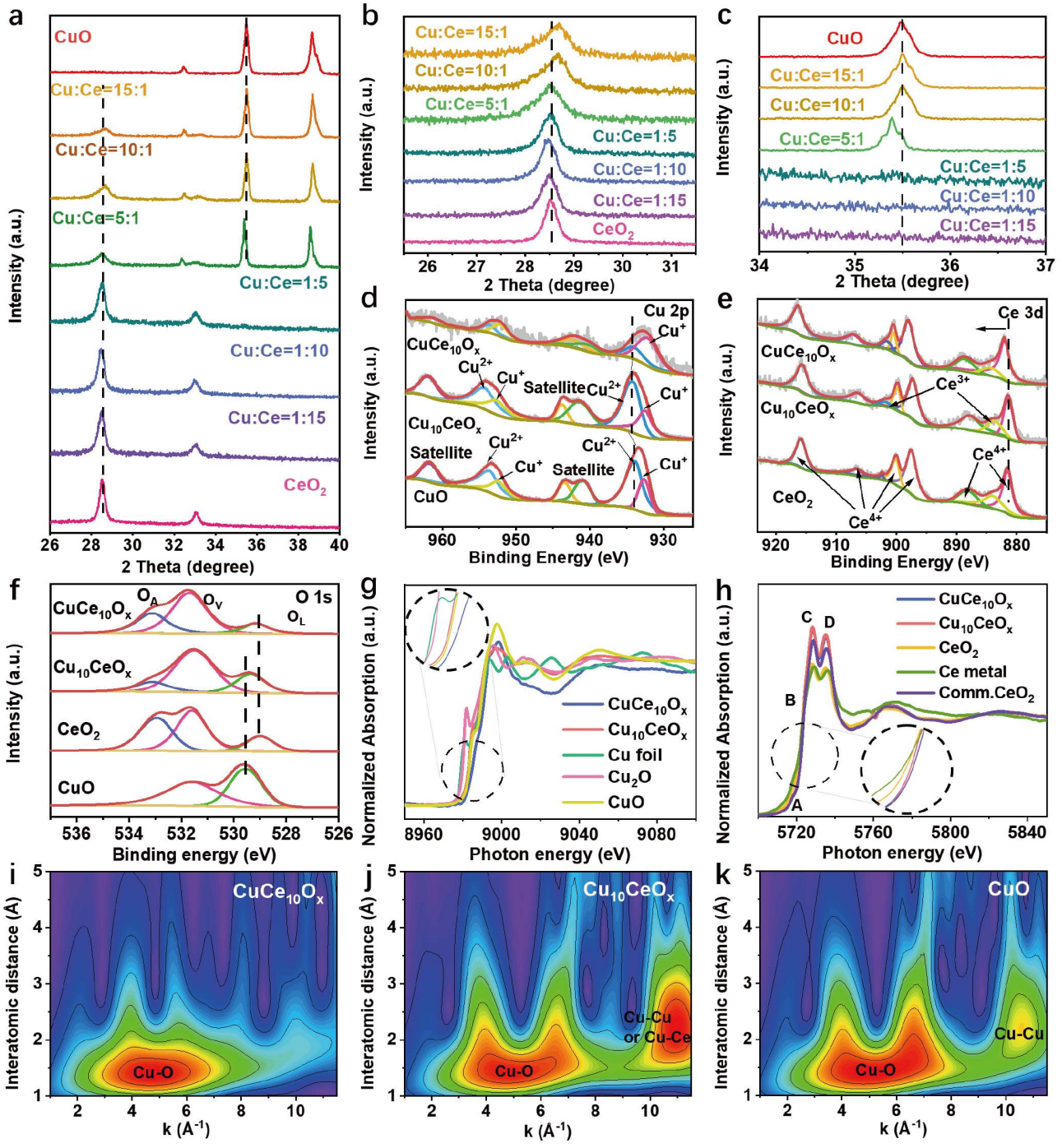


Figure 2 Fine structure characterizations. (a) XRD patterns of catalysts with different feed ratios of Cu to Ce. (b) Magnified XRD patterns of (a) (2θ = 26°–31°). (c) Magnified XRD patterns of (a) (2θ = 34°–37°). High resolution XPS spectra of (d) Cu 2p of $Cu_{10}CeO_x$, $CuCe_{10}O_x$ and CuO, (e) Ce 3d of $Cu_{10}CeO_x$, $CuCe_{10}O_x$ and CeO_2, and (f) O 1s of $Cu_{10}CeO_x$, $CuCe_{10}O_x$, CeO_2 and CuO. (g) Cu K-edge XANES spectra of $Cu_{10}CeO_x$, $CuCe_{10}O_x$, CuO and references. (h) Ce K-edge XANES spectra of $Cu_{10}CeO_x$, $CuCe_{10}O_x$, CeO_2 and references. The WT EXAFS of (i) $CuCe_{10}O_x$, (j) $Cu_{10}CeO_x$ and (k) CuO.

crystal phase with lattice parameters a = 4.6893, b = 3.4268, and c = 5.1321 (PDF#80-1917), while pristine CeO_2 adopts a cubic fluorite structure with the space group *Fm*-3*m* (225) (PDF#81-0792). As shown in Fig. 2b, c, as the Cu/Ce molar ratio increases from 1:15 to 1:10, the XRD diffraction peaks shift toward lower 2θ angles, with no detectable peaks attributable to CuO. This indicates the incorporation of Cu into the CeO_2 lattice, leading to the formation of a Cu–Ce–O solid solution. When the Cu/Ce molar ratio is further increased to 1:5, the XRD peaks shift back to positions similar to those of pristine CeO_2, suggesting the formation of a $CuCeO_x$/CuO composite. At a Cu/Ce ratio of 5:1, two distinct sets of diffraction patterns corresponding to CuO and CeO_2 are observed. Notably, the CeO_2 peaks exhibit a slight shift toward lower 2θ angles, while the CuO peaks display a pronounced negative shift. This implies that a small amount of Ce has been incorporated into the CuO lattice, resulting in a

© The Author(s) 2026. This article is published with open access at link.springer.com.

CeO_2/$CuCeO_x$ composite structure. As the Cu/Ce molar ratio is further increased from 10:1 to 15:1, the diffraction peaks of CeO_2 show a positive shift, while no significant peak displacement is observed for CuO, suggesting the coexistence of CeO_2 and CuO phases. The lattice strain between CeO_2 and CuO accounts for the observed lattice compression of CeO_2 [20]. Based on the XRD shift, the cell parameters of CeO_2 phase in CeO_2, $CuCe_{10}O_x$, and $Cu_{10}CeO_x$ are calculated with a = 5.41656, 5.41385, and 5.41794 Å respectively, which is visually evident for lattice change (Table S1).

To investigate the evolution of the surface electronic structure across different catalyst architectures, X-ray photoelectron spectroscopy (XPS) and X-ray absorption spectroscopy were performed. All XPS spectra were calibrated by referencing the C 1s peak at 284.6 eV. As shown in Fig. S7, distinct peaks corresponding to Ce species were observed in the full XPS spectra of both $CuCe_{10}O_x$ and $Cu_{10}CeO_x$ within the binding energy range of 880–920 eV. A pronounced Cu signal was detected around 930 eV, and multiple O 1s peaks were identified near 530 eV. No additional impurity peaks were observed, confirming that only Cu, Ce, and O species are present on the catalyst surfaces. Further analysis of the oxidation states of each element was carried out using high-resolution XPS. As shown in Fig. 2d, the Cu 2p orbital signals of the pure CuO sample showed that the binding energies of Cu $2p_{1/2}$ and Cu $2p_{3/2}$ located at 953.7 and 933.9 eV, respectively, which correspond to the Cu^{2+} [21]. While the two peaks at 952.3 and 932.7 eV can be indexed to Cu^+. The other three peaks located at 940.2, 943.1 and 962.9 eV are attributed to their satellite peaks of Cu^{2+} [22]. In the Cu 2p XPS spectrum of $Cu_{10}CeO_x$, the peaks corresponding to Cu^+ are located at positions similar to those in CuO. However, the peaks associated with Cu^{2+} exhibit a relatively larger area and are slightly shifted toward higher binding energies compared to those in CuO. In contrast, the Cu 2p spectrum of $CuCe_{10}O_x$ indicates that copper is primarily in the Cu^+ state, as evidenced by the dominant peak area. Therefore, although both Cu^+ and Cu^{2+} species coexist in the Cu-Ce system, $Cu_{10}CeO_x$ is predominantly in the +2 valence state, whereas $CuCe_{10}O_x$ exists mainly in the +1 valence state.

Fig. 2e displays the Ce 3d XPS spectra of CeO_2, $CuCe_{10}O_x$, and $Cu_{10}CeO_x$. In pristine CeO_2, the two peaks located at 881.6 and 897.5 eV correspond to Ce^{4+}, whereas the peaks at 884.2 and 900.1 eV are characteristic of Ce^{3+}, indicating the coexistence of both oxidation states. In particular, the Ce^{3+}/Ce^{4+} ratio in $Cu_{10}CeO_x$ is approximately 16.57%, while it is 11.25% for $CuCe_{10}O_x$, as determined by peak area integration. The presence of Ce^{3+} leads to a charge imbalance in the system and promotes the formation of oxygen vacancies [16,23]. For $Cu_{10}CeO_x$, the Ce 3d XPS peaks a noticeable shift toward higher binding energies, reflecting a reduction in electron density that can be ascribed to strong interactions between CuO and CeO_x. In the case of $CuCe_{10}O_x$, the shift further to higher binding energies suggests a distinct structural configuration compared to $Cu_{10}CeO_x$ and a more pronounced decrease in the electron density of Ce. As shown in Fig. 2f, the O 1s XPS spectrum of CuO can be deconvoluted into two peaks located at binding energies of 529.5 and 531.6 eV, corresponding to lattice oxygen (O_L) and oxygen vacancies (O_V), respectively [24–27]. For pristine CeO_2, the O_L peak appears at 529.0 eV, accounting for 14.98% of the peak's total area, while the O_V peak at 531.6 eV accounts for 45.47%, indicating abundant oxygen vacancies in the CeO_2 structure. Additionally, the peak observed at 532.9 eV is attributed to adsorbed oxygen-containing species, constituting 39.55% of the spectrum. In the case of $Cu_{10}CeO_x$, besides the shift in peak positions, the proportion of O_V increases to 64.51%, suggesting a greater concentration of oxygen vacancies compared to pristine CeO_2—a consequence of induced lattice strain. The corresponding O_L ratio is 22.25%. In contrast, the O_L ratio in $CuCe_{10}O_x$ is even lower than that in $Cu_{10}CeO_x$, further confirming CeO_2 as the host phase and supporting the role of Cu incorporation, whose smaller ionic radius introduces lattice strain and promotes the formation of additional oxygen vacancies [28]. Notably, all catalysts synthesized via the molten salt method exhibit a consistent presence of a substantial number of oxygen vacancies [29].

Fig. 2g displays the K-edge XANES spectra of CuO, $Cu_{10}CeO_x$, $CuCe_{10}O_x$, and commercially available reference samples. Clearly, the synthesized CuO exhibits a positive shift in the K-edge position relative to the commercial CuO. The $Cu_{10}CeO_x$ catalyst shows a K-edge similar to that of pure CuO, whereas $CuCe_{10}O_x$ presents a positively shifted absorption edge compared to the CuO. This shift is attributed to the incorporation of Cu into the CeO_2 lattice. The distinct Cu valence states observed in $Cu_{10}CeO_x$ and $CuCe_{10}O_x$ further highlight their structural differences. The Ce L_3-edge XANES spectra of $Cu_{10}CeO_x$, $CuCe_{10}O_x$, CeO_2, and commercial references are presented in Fig. 2h. All samples—$Cu_{10}CeO_x$, $CuCe_{10}O_x$, and CeO_2—exhibit four characteristic peaks of CeO_2, labeled as A, B, C, and D. Peak A, originating from a dipole-forbidden $2p_{3/2} \rightarrow 4f$ transition, arises due to cubic crystal-field splitting of the Ce 5d states [30]. The main peak C belongs to the transition from Ce 2p to the Ce $4f^1 5d^*L$ configuration (where L denotes an oxygen ligand 2p hole). The high-energy peak D is associated with the final state of core-excited Ce^{4+}, while the low-energy shoulder B is attributed to Ce^{3+} [16]. These features indicate the coexistence of Ce^{3+} and Ce^{4+}, along with a significant number of oxygen vacancies. Moreover, the peak intensities of C and D for $Cu_{10}CeO_x$ and $CuCe_{10}O_x$ are higher than those for pure CeO_2, suggesting increased structural disorder and coordination disturbance in the copper-containing samples. Wavelet transform (WT)-EXAFS spectroscopy was employed to investigate the local atomic structure of copper in $CuCe_{10}O_x$ and $Cu_{10}CeO_x$ catalysts. As shown in Fig. 2i, j, the WT-EXAFS spectra of the two catalysts exhibit distinct features. In the case of $CuCe_{10}O_x$, only one intensity maximum is observed at k = 4.8 $Å^{-1}$, corresponding to the Cu–O interaction. In contrast, for $Cu_{10}CeO_x$, two intensity maxima are present at k = 5.25 and 10.9 $Å^{-1}$, which can be attributed to Cu–O and Cu–Cu/Ce interactions, respectively. The spectral profile of $Cu_{10}CeO_x$ resembles that of pristine CuO (Fig. 2k), providing further evidence that CuO acts as the host structure for Ce doping.

Fig. 3a presents the Fourier-transformed extended XAFS spectra of CuO, $Cu_{10}CeO_x$, $CuCe_{10}O_x$, and commercially available reference samples. A magnified view of the local region between 0–3.0 Å is provided in Fig. S8. In the synthesized CuO sample, the main peak at 1.53 Å corresponds to the first coordination shell of Cu–O, while the peak near 2.75 Å is attributed to the second coordination shell involving Cu–Cu interactions. In contrast, for $Cu_{10}CeO_x$, the first-shell Cu–O peak shifts positively to 1.55 Å, an increase of 0.02 Å compared to pure CuO, while the second coordination shell peak also shifts to a larger interatomic distance of 2.92 Å. These shifts are attributed

© The Author(s) 2026. This article is published with open access at link.springer.com.

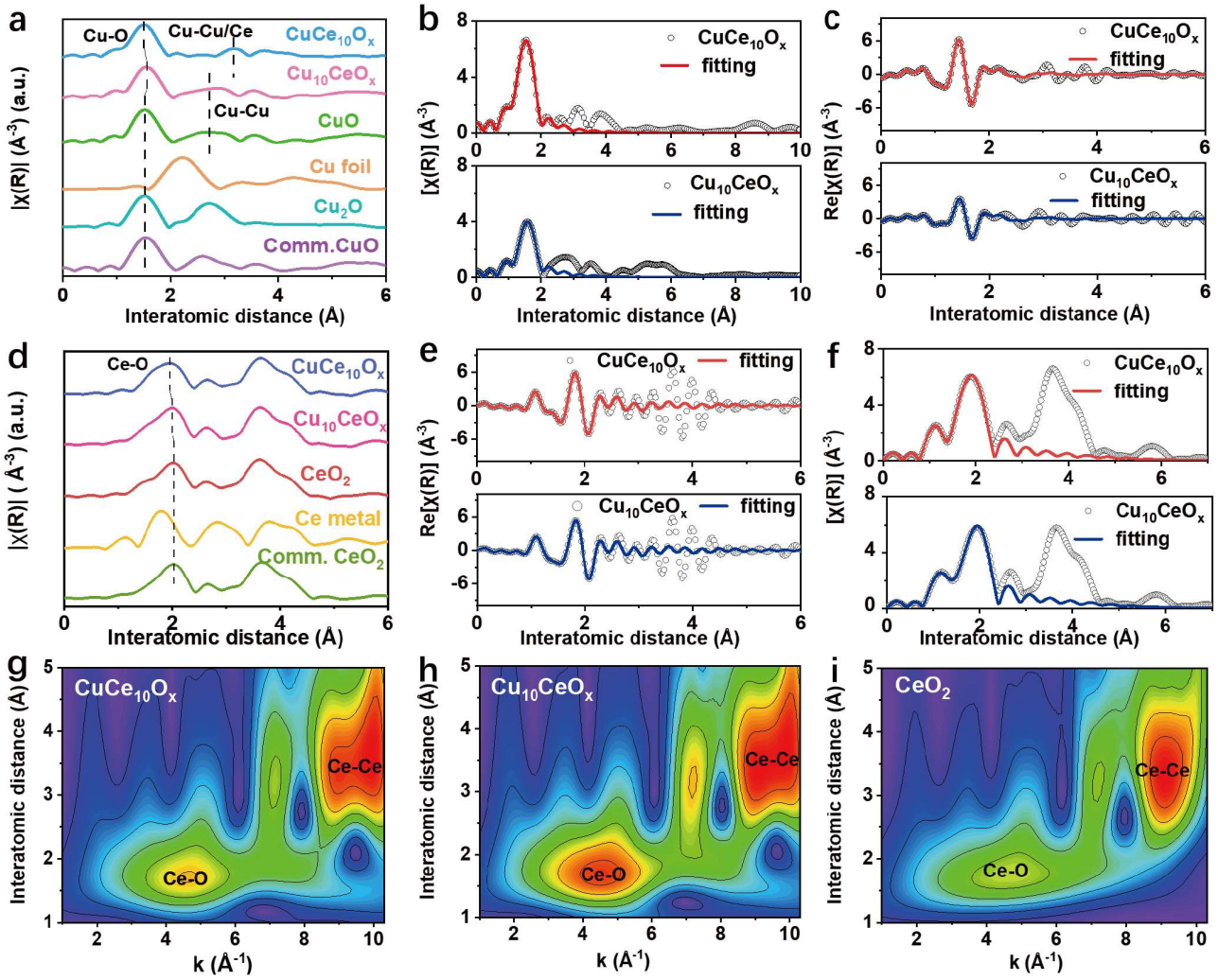


Figure 3 Fine structure characterizations. (a) Cu K-edge FT-EXAFS spectra of $Cu_{10}CeO_x$, $CuCe_{10}O_x$, CeO_2, CuO and commercial references. (b) EXAFS R-space fitting curves of $Cu_{10}CeO_x$ and $CuCe_{10}O_x$. (c) EXAFS fitting profiles at the K-space of $Cu_{10}CeO_x$ and $CuCe_{10}O_x$. (d) Ce K-edge FT-EXAFS spectra of $Cu_{10}CeO_x$, $CuCe_{10}O_x$, and commercial references. (e) EXAFS R-space fitting curves of $Cu_{10}CeO_x$ and $CuCe_{10}O_x$. (f) EXAFS fitting profiles at the K-space of $Cu_{10}CeO_x$ and $CuCe_{10}O_x$. The WT EXAFS of (g) $CuCe_{10}O_x$, (h) $Cu_{10}CeO_x$ and (i) CeO_2.

to lattice strain induced at the CuO–CeO_2 interface. As for $CuCe_{10}O_x$, the Cu–O peak exhibits a negative shift relative to $Cu_{10}CeO_x$, located at 1.50 Å. Meanwhile, the second-shell peak is centered at 3.18 Å, indicating a pronounced increase in interatomic distance compared to $Cu_{10}CeO_x$. This suggests that Cu atoms occupy Ce sites, leading to the formation of a Cu–O–Ce local structure. Through quantitative fitting of the EXAFS spectra in k- and R-space, the structural parameters of the synthesized catalyst were determined (Fig. 3b, c, Fig. S9 and Table S2). In pure CuO, the average coordination number of Cu–O is 4.0, with an average bond length of 1.955 Å. Upon incorporation of a small amount of Ce to form the $Cu_{10}CeO_x$ composite, the Cu–O coordination number decreases to 2.4, while the average bond length increases to 1.965 Å. In contrast, for $CuCe_{10}O_x$, the Cu–O coordination number is 3.9, with an average bond length of 1.948 Å. Previous studies indicate that a reduced coordination number implies a higher electron density in the copper center, with the d-band center closer to the Fermi level. This facilitates feedback π-bonding with the π* antibonding orbitals of reaction intermediates such as *CO, thereby enhancing adsorption and stabilizing key intermediates. The prolonged residence time of *CO on the catalyst surface increases the coupling probability of *CO, driving the reaction towards C_2 products. Conversely, the higher Cu^+/Cu^{2+} ratio results in moderate *CO adsorption strength [31].

The variations in the local coordination structure of Ce were further identified from the near-edge peaks in the Cu–Ce system. As illustrated in Fig. 3d, the as-prepared CeO_2 exhibits two dominant peaks at 2.00 and 3.62 Å, corresponding to the first coordination shell of Ce–O and the second coordination shell of Ce–Ce, respectively. In $Cu_{10}CeO_x$, both the Ce–O and Ce–Ce peaks show a negative shift of approximately 0.02 Å compared to those in CeO_2. In contrast, for $CuCe_{10}O_x$, the peak located at 1.94 Å—shifted negatively by about 0.04 Å relative to $Cu_{10}CeO_x$—is attributed to Ce–O–Cu interactions, while the Ce–Ce/Cu peak appears at 3.63 Å. Quantitative EXAFS curve fitting analyses (in both k and R spaces) were performed to further elucidate the evolution of the coordination microenvironment in $CuCe_{10}O_x$ and $Cu_{10}CeO_x$ (Fig. 3e, f, Fig. S10, and Table S3). In the prepared CeO_2, the average coordination number of Ce–O is 4.7, with a mean bond length of 2.342 Å. For $Cu_{10}CeO_x$, the coordination number of the Ce–O scattering path increases to

© The Author(s) 2026. This article is published with open access at link.springer.com.

6.7, and the average bond length becomes 2.338 Å. Meanwhile, in $CuCe_{10}O_x$, the average coordination number and bond length of Ce–O further change to 7.0 and 2.328 Å, respectively. The WT-EXAFS contour plots in Fig. 3g–i and Fig. S11 reveal that the spectra of $CuCe_{10}O_x$ and $Cu_{10}CeO_x$ are similar to that of CeO_2, with a maximum intensity around k = 4.63 $Å^{-1}$ corresponding to the Ce–O scattering path, and another maximum around k = 9.54 $Å^{-1}$ attributed to the Ce–Ce scattering path. However, the scattering peak intensity of the Ce–O path differs between $CuCe_{10}O_x$ and $Cu_{10}CeO_x$. The intensity in $CuCe_{10}O_x$ is closer to that of pure CeO_2, further supporting the conclusion that copper is doped into the host CeO_2 lattice. The nature of the active sites, including their structure and distribution, is critically influenced by the host phase and coordination environment, leading to tailored catalytic performance.

Electrocatalytic CO_2 reduction performance

The impact of the local active site concentration and coordination on the CO_2RR was investigated by evaluating the Cu-Ce catalysts in an anion exchange membrane (AEM)-equipped flow cell. The experimental procedure was as follows: catalysts were pre-activated under constant-current conditions in 1 M KOH. Subsequently, controlled-potential electrolysis was carried out for 1 h at each potential to generate products for analysis (Fig. S12). The gaseous and liquid products were quantified using online gas chromatography (GC; Fig. S13) and 1H nuclear magnetic resonance (NMR; Fig. S14), respectively. To corroborate their intrinsic activity, linear sweep voltammetry (LSV) was conducted in both CO_2- and Ar-saturated 1 M KOH (Fig. S15), confirming that all samples were active for CO_2RR.

A remarkable product selectivity switch is evident between $CuCe_{10}O_x$ and $Cu_{10}CeO_x$ electrodes (Fig. 4a). While $Cu_{10}CeO_x$ directs the CO_2RR toward C_2 products (FE_{C_2max} = 61.5% at −1.4 V vs. RHE), $CuCe_{10}O_x$ shifts the selectivity predominantly to CH_4 (FE_{CH_4max} = 61.7% at −1.6 V vs. RHE). Compared with other catalysts, it exhibits superior selectivity and higher partial current density (Fig. S16). Another key difference is that $Cu_{10}CeO_x$ demonstrates a suppression of methane FE and a promotion of the HER relative to $CuCe_{10}O_x$ during cathodic polarization. We attribute this to the kinetically challenging C_2 pathway, which requires multi-electron/proton transfers and precise intermediate adsorption/desorption kinetics [32]. This pathway becomes especially vulnerable to suppression by the competing HER at elevated overpotentials. Additionally, CeO_2 demonstrates dominant HER behavior (>90% Faradaic efficiency across all applied potentials), highlighting its effectiveness in generating active hydrogen species (*H) (Fig. S17). According to our previous study, Ce-O_V is the dominant active site for water adsorption and promotes water dissociation [16]. This feature allows for strategic control over intermediate concentrations by tuning the structural configuration of CeO_2–CuO composites, thereby directing reaction pathways toward selective product formation. The structural design plays a critical role in determining ECO_2RR product selectivity. To clarify the origin of the selectivity switch between $CuCe_{10}O_x$ and $Cu_{10}CeO_x$, controlled experiments with varying Cu/Ce ratios were conducted (Fig. 4b, c). The results reveal a volcano-shaped dependence of CH_4 selectivity on Ce content, whereas C_2H_4 selectivity follows a similar non-monotonic trend with increasing Cu loading (Fig. 4d). Besides, the holding time has no significant effect on performance (Fig. S18).

The partial current densities for C_2 (j_{C_2}) and CH_4 (j_{CH_4}) were calculated based on Faradaic efficiencies and total current densities (Fig. 4e, f). Notably, $CuCe_{10}O_x$ exhibits a significantly higher j_{CH_4} than $Cu_{10}CeO_x$, with a maximum value of −199.18 mA cm^{-2} at −1.7 V vs. RHE. This enhancement is attributed to the greater abundance of Ce–O_V sites in the Cu–Ce solid-solution structure, which facilitates the generation of more active hydrogen species and increases the *H coverage around Cu sites, thereby promoting the hydrogenation process. In contrast, $Cu_{10}CeO_x$ demonstrates a considerably larger j_{C_2} compared to $CuCe_{10}O_x$, reaching a maximum of −223.49 mA cm^{-2} at −1.4 V vs. RHE. These findings further corroborate that the local concentration of active sites plays a critical role in determining the product selectivity in the CO_2 reduction. Cyclic voltammetry (CV) measurements were conducted at various scan rates to determine the double-layer capacitance (C_{dl}) (Fig. 4g and Fig. S19). The C_{dl} values of four representative samples reveal an interesting trend: the C_{dl} of $CuCe_{10}O_x$ is similar to that of CeO_2, while that of $Cu_{10}CeO_x$ is close to CuO, indicating that the double-layer capacitance is governed by the host phase. Nevertheless, the C_{dl} of $CuCe_{10}O_x$ is slightly higher than that of CeO_2, and similarly, $Cu_{10}CeO_x$ exhibits a marginally larger C_{dl} than CuO. This can be attributed to the formation of additional vacancies, which help expose more active sites—some of which may themselves serve as active centers. To achieve a more accurate quantification of the Cu sites, CO stripping experiments and inductively coupled plasma (ICP) measurements were conducted (Fig. S20) to obtain the inherent concentration and electrochemically accessible concentration, respectively. Evidently, the inherent concentration of Cu is 9.112 μmol mg^{-1} for $Cu_{10}CeO_x$ and 0.693 μmol mg^{-1} for $CuCe_{10}O_x$, while electrochemically accessible concentration is 0.061 μmol mg^{-1} for $Cu_{10}CeO_x$ and 0.007 μmol mg^{-1} for $CuCe_{10}O_x$. Partial current density normalized to copper surface sites was also evaluated, as shown in Fig. S21. Furthermore, electrochemical impedance spectra (Fig. 4h) show a significant reduction in charge transfer resistance for both $CuCe_{10}O_x$ and $Cu_{10}CeO_x$, suggesting enhanced charge transfer kinetics relative to the pure metal oxides. The corresponding equivalent circuit is shown in Fig. S22. Two possible factors may explain this improvement: the presence of oxygen vacancies and lattice strain that alter the relative positions of the Fermi level with respect to the conduction and valence bands. Critically, at −1.7 V vs. RHE (Fig. 4i, j), $CuCe_{10}O_x$ delivers a methane production rate (PR_{CH_4}) of 929 μmol s^{-1} cm^{-2}, surpassing that of $Cu_{10}CeO_x$ by a factor of 21.6. In contrast, $Cu_{10}CeO_x$ shows superior ethylene productivity (PR_{C_2} = 704.37 μmol s^{-1} cm^{-2}), exceeding that of $CuCe_{10}O_x$ (82.46 μmol s^{-1} cm^{-2}) by 6.31 times. Moreover, both $CuCe_{10}O_x$ and $Cu_{10}CeO_x$ demonstrate good electrocatalytic stability (Fig. S23), maintaining FE_{CH_4} above 50% and $FE_{C_2H_4}$ above 38% over 11 h, at average current densities of approximately −325 and −415 mA cm^{-2}, respectively.

Catalytic mechanism study

Due to the inherent instability of $*CO_2$ in the electrolyte environment, the adsorption capacity of *OH was evaluated through a single oxidative voltammetric scan as an indirect measure of $*CO_2$ retention on the catalyst surface. As shown in Fig. 5a, the $CuCe_{10}O_x$ catalyst exhibited a lower *OH adsorption potential than $Cu_{10}CeO_x$. The result suggests that $Cu_{10}CeO_x$ possesses a stronger binding affinity for $*CO_2$, which enhances

© The Author(s) 2026. This article is published with open access at link.springer.com.

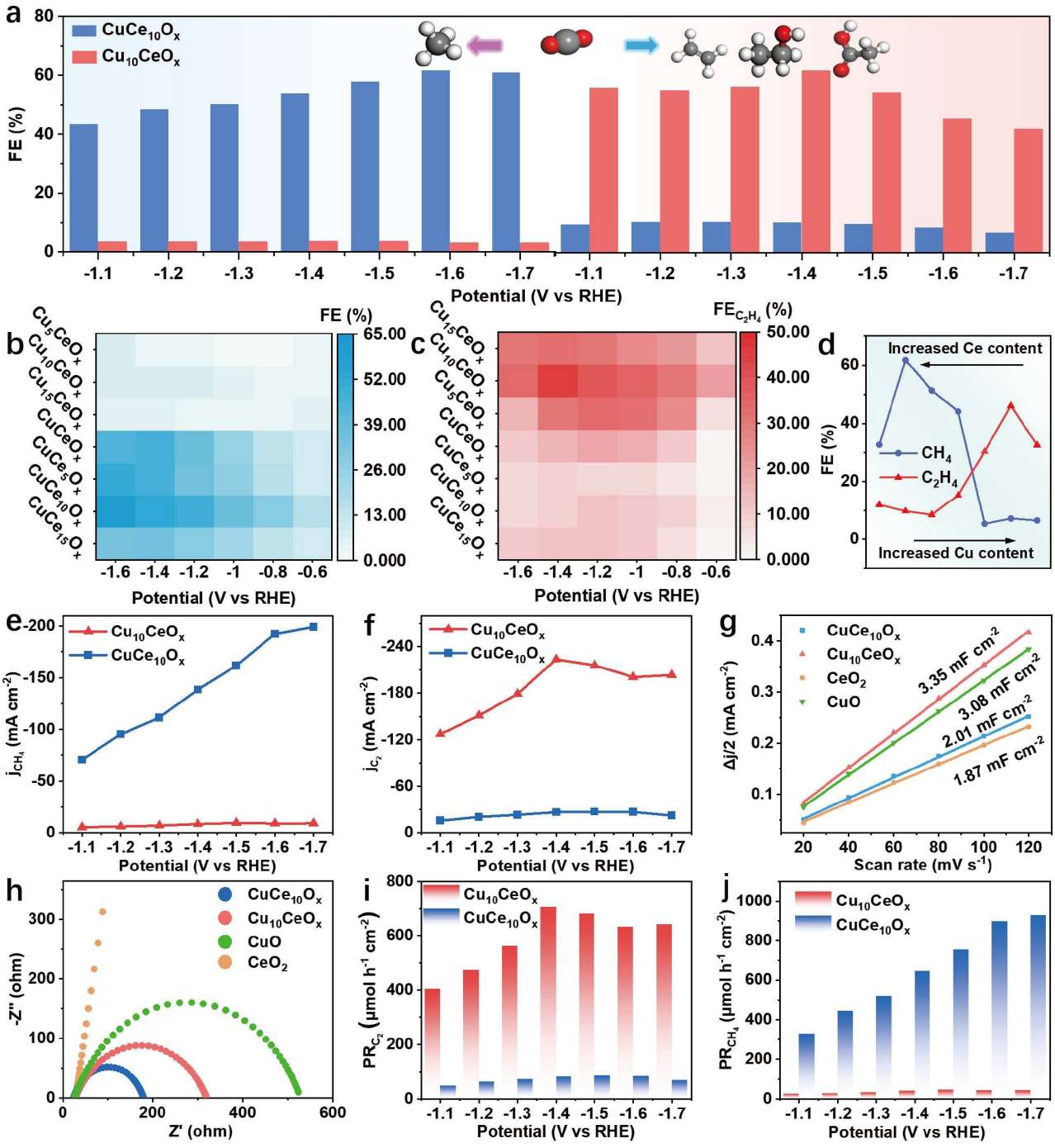


Figure 4 Switching CO_2RR selectivity. (a) FEs of the CH_4 (left) and C_2H_4 (right) over $CuCe_{10}O_x$ (blue) and $Cu_{10}CeO_x$ (red) at applied potentials. (b) FE_{CH_4} and (c) $FE_{C_2H_4}$ of catalysts with different molar ratio of Cu to Ce. (d) FEs of CH_4 and C_2H_4 with the variation of element content. (e) Partial CH_4 current densities and (f) partial C_2 current densities of $Cu_{10}CeO_x$ and $CuCe_{10}O_x$. (g) C_{dl} values and (h) electrochemical impedance spectra of $Cu_{10}CeO_x$, $CuCe_{10}O_x$, CeO_2 and CuO. Production rates of (i) C_2 and (j) CH_4 as measured over $Cu_{10}CeO_x$ and $CuCe_{10}O_x$ catalysts.

*CO surface coverage and creates favorable conditions for C–C coupling reactions [10]. To investigate whether *H coverage on the catalysts influences product selectivity, surface *H trapping experiments were conducted using *t*-BuOH as the *H trapping agent (Fig. 5b, c). Upon the addition of *t*-BuOH, the current densities decreased for both catalysts. Notably, the $FE_{CH_4}/FE_{C_2H_4}$ ratio of $CuCe_{10}O_x$ decreased more significantly than that of $Cu_{10}CeO_x$ under the same conditions, suggesting that CH_4 formation is more sensitive to the availability of surface *H species. In the $CuCe_{10}O_x$ catalyst, the CeO_2 host phase provides an abundant supply of *H, facilitating the further protonation of the *CO intermediate and thereby promoting CH_4 production [33]. Although the use of *t*-BuOH as a hydrogen scavenger may indeed introduce additional effects by altering local pH and double-layer structure, it still can support our above conclusion as to its low concentration. At this concentration, local pH variations (≤0.5 units) exerted a negligible influence on the CO_2 reduction reaction pathways of the catalyst, with the primary

© The Author(s) 2026. This article is published with open access at link.springer.com.

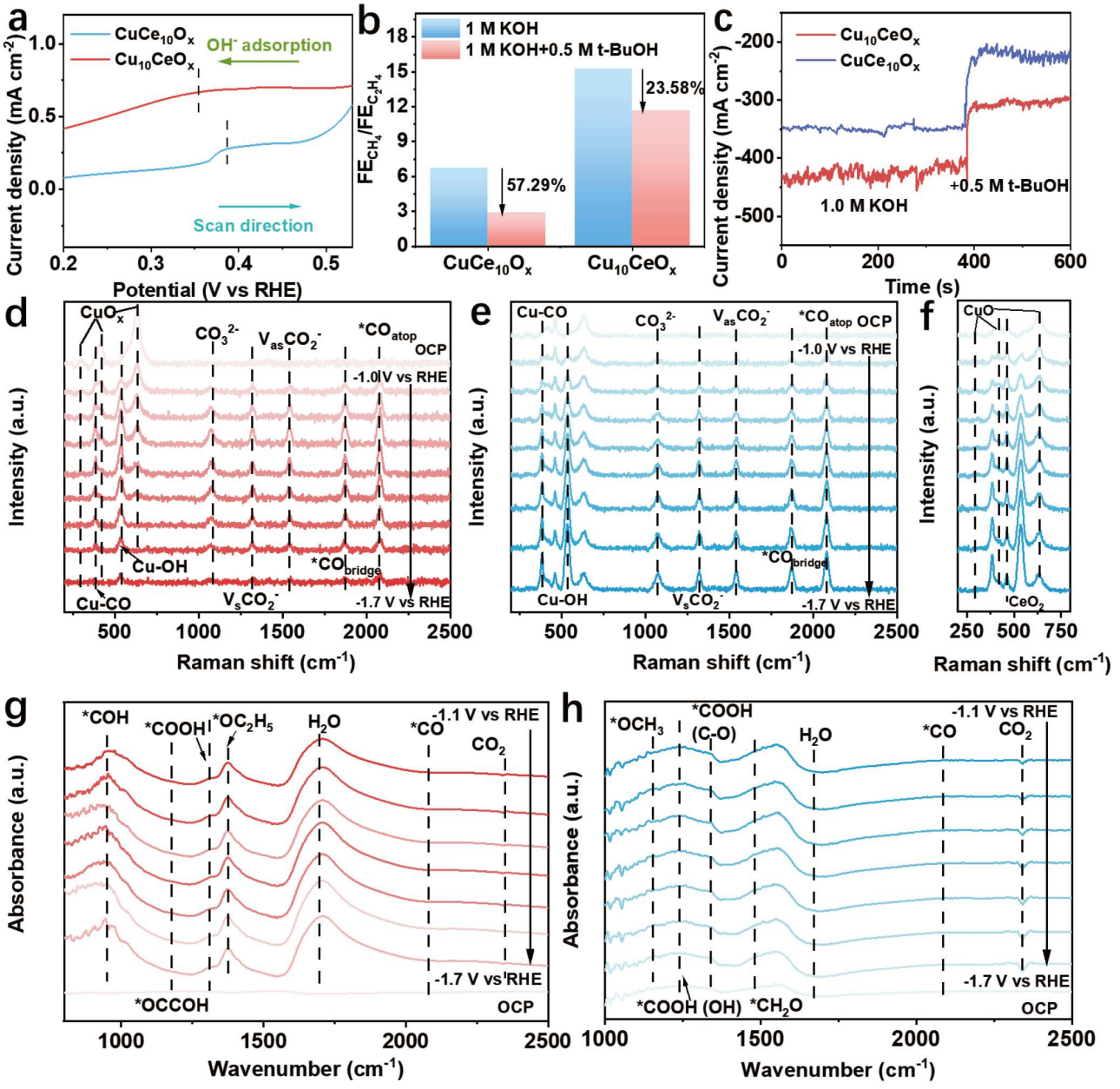


Figure 5 Catalytic mechanism study. (a) Single oxidative LSV scans of different samples at 50 mV s^{-1} in Ar-saturated 0.1 M KOH. (b) Ratio of $FE_{CH_4}/FE_{C_2H_4}$ on $CuCe_{10}O_x$ at the constant voltage of −1.6 V vs. RHE and $Cu_{10}CeO_x$ at the constant voltage of −1.4 V vs. RHE in a CO_2-saturated 0.1 M KOH solution with and without the addition of 0.5 M *t*-BuOH. (c) Current density-time curves of $CuCe_{10}O_x$ at −1.6 V vs. RHE and $Cu_{10}CeO_x$ at −1.4 V vs. RHE in a CO_2-saturated 1 M KOH solution with and without the addition of 0.5 M *t*-BuOH. *In situ* Raman spectra under different potentials over (d) $Cu_{10}CeO_x$ and (e, f) $Cu_{10}CeO_x$. *In situ* ATR-FTIR spectra recorded at different potentials for (g) $Cu_{10}CeO_x$ and (h) $CuCe_{10}O_x$.

product remaining unchanged.

To gain deeper insights into the reaction mechanism, we systematically employed *in-situ* Raman spectroscopy and attenuated total reflection FTIR spectroscopy (ATR-FTIR) to identify potential intermediates formed during the CO_2RR. As shown in Fig. 5d–f, Raman spectra of the as-prepared working electrode were collected at various applied potentials, revealing changes in the chemical environment associated with the electrochemical process. Under open-circuit potential (OCP) conditions, both $CuCe_{10}O_x$ and $Cu_{10}CeO_x$ exhibit characteristic Raman peaks for Cu–O species at 295, 414, and 637 cm^{-1} [34,35]. With increasingly negative applied potentials, these peaks gradually disappear in $Cu_{10}CeO_x$, indicating the reduction of CuO species to metallic copper [36]. In contrast, the Cu–O vibrational features in $CuCe_{10}O_x$ remain largely unchanged, demonstrating that the introduction of a high cerium content effectively stabilizes the copper species against reduction. At a potential of −1.7 V vs. RHE, the Cu^{2+}/Cu^{+} ratio reaches its optimum for CH_4 production, with the Cu–CO peak intensity peaking at this point, corresponding to the maximum CH_4 Faradaic efficiency. The persistent presence of the v(Cu-CO/*CO_2) peaks at 382, 1318, and 1540 cm^{-1}, indicates excellent *CO_2 adsorption behavior on both $CuCe_{10}O_x$ and $Cu_{10}CeO_x$, thereby promoting reactant activation [37,38]. Moreover, the H_2O peak intensity for

© The Author(s) 2026. This article is published with open access at link.springer.com.

$CuCe_{10}O_x$ shifts downward, which can be attributed to the rapid consumption of water on the catalyst surface. This observation aligns with the previously noted strong water dissociation capability of CeO_2, which creates more favorable conditions for the protonation of the *CO intermediate. The Cu–CO peak intensity is stronger in the $CuCe_{10}O_x$ spectrum, demonstrating that $Cu_{10}CeO_x$ exhibits superior C–C coupling capability and a higher tendency to form multi-carbon products [39]. As shown in Fig. 5g, h, the infrared spectra of the working electrodes fabricated from $CuCe_{10}O_x$ and $Cu_{10}CeO_x$ were recorded at different applied potentials. A distinct absorption band at 1325 cm^{-1}, observed for both $CuCe_{10}O_x$ and $Cu_{10}CeO_x$, is assigned to *COOH—commonly identified as a key intermediate in the electrochemical CO_2 reduction reaction. In the spectrum of $CuCe_{10}O_x$, additional peaks at 1152 and 1483 cm^{-1} are attributed to $*OCH_3$ and $*CH_2O$, respectively [40]. These species are critical precursors for methane formation and are consistent with the catalyst's highest Faradaic efficiency for CH_4.

In contrast, the *in situ* IR spectrum of $Cu_{10}CeO_x$ exhibits that a less prominent characteristic peak observed at approximately 1180 cm^{-1} can be assigned to the *OCCOH reaction intermediates, indicating C–C bond formation through the asymmetric coupling of adsorbed *CO and *COH species [41–43]. Moreover, the inverted adsorption peaks of H_2O observed for $CuCe_{10}O_x$, in sharp contrast to those of $Cu_{10}CeO_x$, further indicate the rapid consumption of water molecules without sufficient replenishment, strongly evidencing the high water dissociation capability of CeO_2. Although similar inverted adsorption peaks are observed for CO_2, the underlying reason differs from that of H_2O. In the case of CO_2, the phenomenon is attributed to the weak adsorption capacity of $CuCe_{10}O_x$, resulting from the limited number of Cu active sites.

DFT calculations were performed to deepen the understanding of the reaction mechanism. To further demonstrate that the enhanced *H coverage and water dissociation are attributable to Ce–O_V sites, theoretical calculations were performed on the water dissociation process over $CuCe_{10}O_x$. Fig. 6a demonstrates that oxygen vacancies significantly enhance water

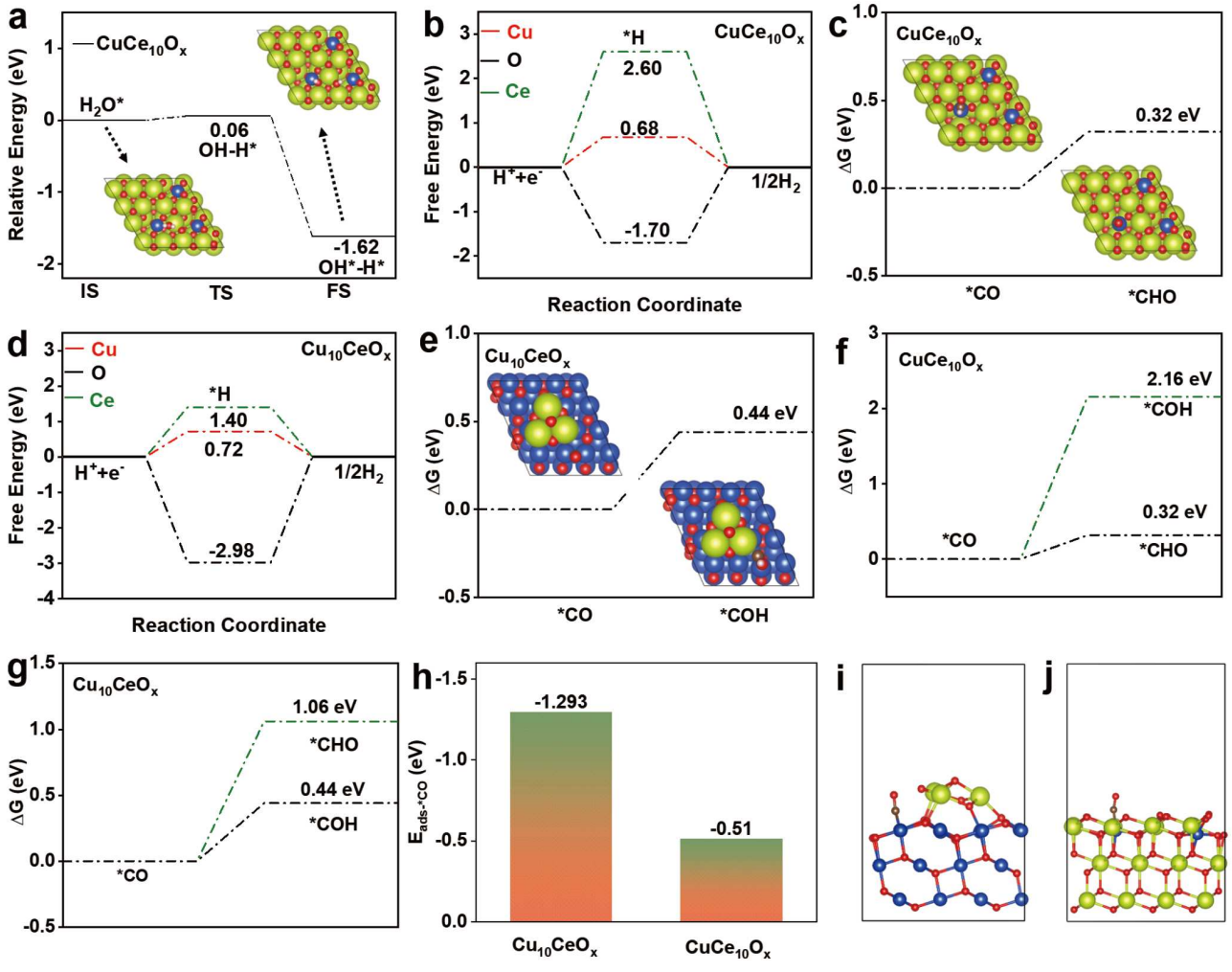


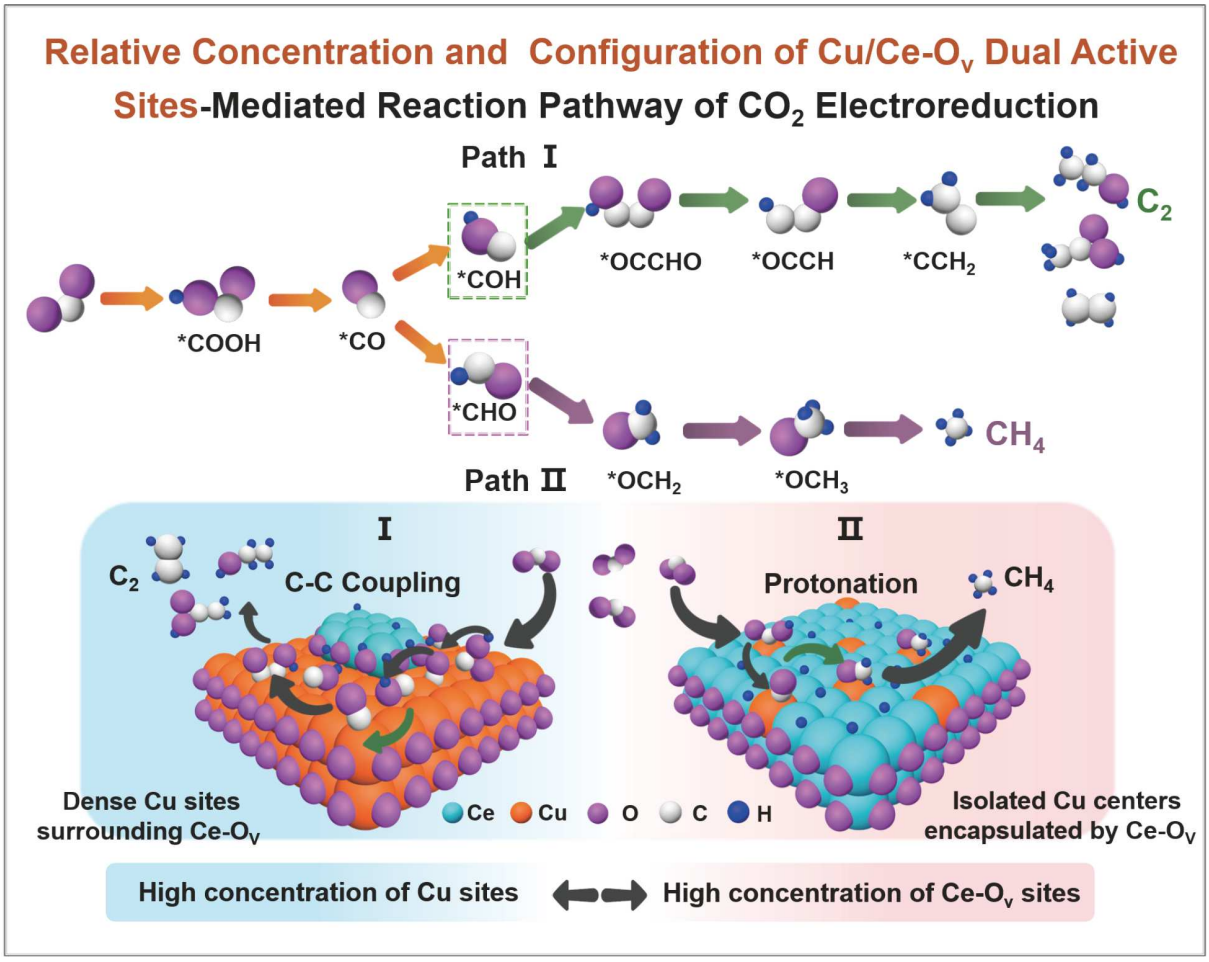
Figure 6 DFT calculations. (a) Kinetic barrier of water dissociation on the surface active sites of $CuCe_{10}O_x$. IS, TS, and FS represent the initial, transition state, and final state, respectively. (b) Calculated adsorption free energies of H on various sites in $CuCe_{10}O_x$. (c) Calculated free energy barriers for *CO to *CHO conversion on $CuCe_{10}O_x$, with corresponding adsorption configurations: *CO adsorbed on the Cu site and *CHO adsorbed on the Cu site. (d) Calculated adsorption free energies of *H on various sites in $Cu_{10}CeO_x$. (e) Calculated free energy barriers for the *CO to *COH conversion on $Cu_{10}CeO_x$, along with the corresponding adsorption configurations: adsorbed *CO and adsorbed *COH. (f) Calculated free energy barriers for the *CO-to-*COH/*CHO conversion over $CuCe_{10}O_x$. (g) Calculated free energy barriers for the *CO-to-*COH/*CHO conversion on $Cu_{10}CeO_x$. (h) Calculated *CO adsorption energies on $Cu_{10}CeO_x$ and $CuCe_{10}O_x$, along with their corresponding adsorption configurations: adsorbed *CO on (i) $CuCe_{10}O_x$ and (j) $Cu_{10}CeO_x$.

© The Author(s) 2026. This article is published with open access at link.springer.com.

dissociation activity. With an energy barrier of only 0.06 eV for water dissociation, the $CuCe_{10}O_x$ surface efficiently generates abundant active hydrogen species. This rapid hydrogen production effectively promotes deep protonation of the *CHO intermediate, thereby driving its conversion to CH_4.

The Faraday efficiency diagram indicates that the *H provided by the Ce–O_V site does not enhance the HER, but promotes the formation of CO_2 reduction reaction products. Generally, there is a significant competitive relationship between the HER and the CO_2 reduction reaction. In the $CuCe_{10}O_x$ system, excessively strong H adsorption energy at the O sites (−1.70 eV), combined with excessively weak H adsorption energy at the Ce (2.60 eV) and Cu sites (0.68 eV) as shown in Fig. 6b and Fig. S24a–c, jointly impedes the proton-electron transfer process, kinetically suppressing HER. This creates favorable conditions for the hydrogenation pathway of carbon-containing intermediates. Specifically, on the Cu active sites, the energy barrier for *CO hydrogenation to form *CHO is as low as 0.32 eV (Fig. 6c), which is significantly lower than the kinetic barrier for HER. This drives the reaction toward the continuous hydrogenation pathway to produce CH_4, rather than releasing H_2. In the $Cu_{10}CeO_x$ system, the strong H adsorption at O sites (−2.98 eV) and weak adsorption at Ce (1.40 eV) and Cu (0.72 eV) sites (Fig. 6d and Fig. S24d–f) jointly suppress HER by impeding proton-electron transfer, thus favoring hydrogenation of carbon-containing intermediates. Specifically, the barrier for *CO hydrogenation to *COH is only 0.44 eV (Fig. 6e), significantly lower than that for HER, directing the reaction toward continuous hydrogenation rather than H_2 evolution.

The CO_2RR reaction pathway exhibits multiple possibilities, and computational analysis was performed to confirm the reaction pathway. In the $CuCe_{10}O_x$ catalyst system, methane is the primary product. Computational results indicate that the energy barrier for the *CO hydrogenation pathway to form *CHO is 0.32 eV (Fig. 6f and Fig. S25a–c), which is significantly lower than that of the competing pathway to form *COH (2.16 eV). This suggests that the consecutive hydrogenation pathway via *CHO possesses clear thermodynamic and kinetic advantages, thereby effectively driving the reaction toward CH_4 formation. In contrast, in the $Cu_{10}CeO_x$ catalyst system, ethylene is the dominant product. The energy barrier for the *CO → *COH pathway is only 0.44 eV, notably lower than that of the *CO → *CHO pathway (1.06 eV) (Fig. 6g and Fig. S25d–f). This indicates that the *COH intermediate is more readily formed and accumulated, thereby promoting subsequent C–C coupling and ultimately leading to the formation of C_2 products. This comparison clearly demonstrates how distinct active site structures regulate the energy barriers for the formation of key intermediates (*CHO vs. *COH), thereby governing the selective distribution of products. The adsorption energies of *CO on different catalysts were also calculated. The *CO adsorption energy on $CuCe_{10}O_x$ (−0.51 eV) is weaker than that on



Scheme 1 Schematic of the reaction path modulated by active site concentration.

© The Author(s) 2026. This article is published with open access at link.springer.com.

$Cu_{10}CeO_x$ (−1.29 eV) (Fig. 6h–j). The *CO stripping charge on $Cu_{10}CeO_x$ and $CuCe_{10}O_x$ (Fig. S26) further confirms the high *CO coverage on the $Cu_{10}CeO_x$ surface than on the $CuCe_{10}O_x$. The stronger *CO adsorption on $Cu_{10}CeO_x$ facilitates its retention and subsequent dimerization.

In brief, the local configuration and concentration of active sites critically determine the reaction pathway in CO_2RR, governing ultimate product selectivity (Scheme 1). Specifically, copper sites exhibit higher activity toward *CO species, whereas cerium sites coupled with Ov are more favorable for water dissociation. In $Cu_{10}CeO_x$, the abundance of Cu active sites around Ce–O_V sites results in higher *CO coverage compared to *H coverage. This enhances the probability of collisions among reactive species, facilitating C–C coupling via the formation of an *OCCOH intermediate. In contrast, $CuCe_{10}O_x$ features a surplus of Ce–O_V sites enveloping isolated Cu centers, which favors high *H coverage while limiting *CO availability. As a result, the reaction shifts toward deep hydrogenation pathways.

CONCLUSIONS

In summary, the local configuration and concentration of active sites play a critical role in steering intermediate migration and reaction pathways during CO_2RR, thereby governing product selectivity. We synthesized Cu–O_V–Ce catalysts with tunable relative concentrations and distributions of Cu and Ce–O_V sites via a molten salt-assisted strategy. Aggregated Cu sites around Ce–O_V enhance *CO_2 binding, increase *CO surface coverage, and promote *CO–*COH coupling. In contrast, abundant Ce–O_V sites facilitate water adsorption and dissociation, supplying more active *H to drive deep protonation of *CHO toward CH_4. As a result, $CuCe_{10}O_x$ achieves a CH_4 FE of 61.7% at −1.6 V vs. RHE, while $Cu_{10}CeO_x$ favors C_2 production with an FE of 61.5% at −1.4 V vs. RHE. This work underscores the importance of tailoring the local structure and distribution of active sites to control product selectivity, offering key insights for designing highly selective CO_2 valorization catalysts.

Received 15 December 2025; accepted 3 February 2026; published online 21 May 2026

1 Guan Y, Li Y, Li Z, *et al.* Promotion of C–C coupling in the CO_2 electrochemical reduction to valuable C_{2+} products: from micro-foundation to macro-application. Adv Mater, 2025, 37: 2417567
2 Lu R, Liu Y, Wang Z. Advances in the understanding of selective CO_2 reduction catalysis. EcoEnergy, 2024, 2: 695–713
3 Nielsen DU, Hu XM, Daasbjerg K, *et al.* Chemically and electrochemically catalysed conversion of CO_2 to CO with follow-up utilization to value-added chemicals. Nat Catal, 2018, 1: 244–254
4 Haas T, Krause R, Weber R, *et al.* Technical photosynthesis involving CO_2 electrolysis and fermentation. Nat Catal, 2018, 1: 32–39
5 Zhang H, He C, Han S, *et al.* Crystal facet-dependent electrocatalytic performance of metallic Cu in CO_2 reduction reactions. Chin Chem Lett, 2022, 33: 3641–3649
6 Yan JC, Wang FM, Yin S, *et al.* Copper/metal oxide heterostructures for electrochemical carbon dioxide reduction. Rare Met, 2025, 44: 2239–2267
7 Jan Z, Guo Q, Zhang J, *et al.* Dynamic reconstruction of electrocatalysts during CO_2 reduction reactions. Sci China Chem, 2025, doi: 10.1007/s11426-025-2965-8
8 Zhang R, Kong X, Ren R, *et al.* Recent advances in copper-based catalysts for electrochemical carbon dioxide reduction to C_{2+} products. Carbon Neutralization, 2025, 4: e70041
9 Liu T, Zhao Y, Zhai T. Does a higher density of active sites indicate a higher reaction rate? J Am Chem Soc, 2024, 146: 6461–6465
10 Zhang T, Yuan B, Wang W, *et al.* Tailoring *H intermediate coverage on the $CuAl_2O_4$/CuO catalyst for enhanced electrocatalytic CO_2 reduction to ethanol. Angew Chem Int Ed, 2023, 62: e202302096
11 Wen X, Min Q, Liu X, *et al.* Antireconstruction Cu nanowire catalysts enabled by SiO_2 encapsulation for durable electrochemical CO_2 reduction. ACS Catal, 2025, 15: 14215–14226
12 Jiao J, Kang X, Yang J, *et al.* Steering the reaction pathway of CO_2 electroreduction by tuning the coordination number of copper catalysts. J Am Chem Soc, 2024, 146: 15917–15925
13 Xia C, Wang X, He C, *et al.* Highly selective electrocatalytic CO_2 conversion to tailored products through precise regulation of hydrogenation and C–C coupling. J Am Chem Soc, 2024, 146: 20530–20538
14 Yang T, Kuang M, Yang J. Mesoporous CuCe dual-metal catalysts for efficient electrochemical reduction of CO_2 to methane. Chin J Struct Chem, 2024, 43: 100350
15 Wang H, Kang X, Han B. Rare-earth element-based electrocatalysts designed for CO_2 electro-reduction. ChemSusChem, 2024, 17: e202301539
16 Qin Q, Jang H, Jiang X, *et al.* Constructing interfacial oxygen vacancy and ruthenium Lewis acid–base pairs to boost the alkaline hydrogen evolution reaction kinetics. Angew Chem Int Ed, 2024, 63: e202317622
17 Zhong D, Zhao Z, Zhao Q, *et al.* Coupling of Cu(100) and (110) facets promotes carbon dioxide conversion to hydrocarbons and alcohols. Angew Chem Int Ed, 2021, 60: 4879–4885
18 Feng X, Zou H, Zheng R, *et al.* Bi_2O_3/BiO_2 nanoheterojunction for highly efficient electrocatalytic CO_2 reduction to formate. Nano Lett, 2022, 22: 1656–1664
19 Huang J, Zhang X, Yang J, *et al.* Recent progress on copper-based bimetallic heterojunction catalysts for CO_2 electrocatalysis: unlocking the mystery of product selectivity. Adv Sci, 2024, 11: 2309865
20 Song Y, Ghoridi A, Igoa Saldaña F, *et al.* In and out: shuttling atoms in covalent nanocrystals, from synthesis in molten salts to water-splitting electrocatalysis. J Am Chem Soc, 2025, 147: 20878–20887
21 Wang M, Chen H, Wang M, *et al.* Tuning C_1/C_2 selectivity of CO_2 electrochemical reduction over *in-situ* evolved CuO/SnO_2 heterostructure. Angew Chem Int Ed, 2023, 62: e202306456
22 Li Y, Shi H, Li C, *et al.* Shaping hollow spherical assemblies for enhanced Cu^0/Cu^+ interface to boost C_{2+} selectivity in CO_2 electroreduction. Sci China Mater, 2024, 67: 3596–3601
23 Campbell CT, Peden CHF. Oxygen vacancies and catalysis on ceria surfaces. Science, 2005, 309: 713–714
24 Zhou S, Jang H, Qin Q, *et al.* Boosting hydrogen evolution reaction by phase engineering and phosphorus doping on Ru/P-TiO_2. Angew Chem, 2022, 134: e202212196
25 Qin Q, Wang T, Li Z, *et al.* Tuning electronic structure of RuO_2 by single atom Zn and oxygen vacancies to boost oxygen evolution reaction in acidic medium. J Energy Chem, 2024, 88: 94–102
26 Jiang X, Jang H, Liu S, *et al.* The heterostructure of Ru_2P/WO_3/NPC synergistically promotes H_2O dissociation for improved hydrogen evolution. Angew Chem Int Ed, 2021, 60: 4110–4116
27 Li G, Jang H, Liu S, *et al.* The synergistic effect of Hf–O–Ru bonds and oxygen vacancies in Ru/HfO_2 for enhanced hydrogen evolution. Nat Commun, 2022, 13: 1270
28 Zhao Z, Zhang Y, Li J, *et al.* Enhanced active hydrogen absorption and stabilized Cu(I) species over Cu–O–Ce bridges boosting electrocatalytic CO_2 reduction to ethylene. Angew Chem Int Ed, 2025, 64: e202510383
29 Jiang W, Loh H, Low BQL, *et al.* Role of oxygen vacancy in metal oxides for photocatalytic CO_2 reduction. Appl Catal B-Environ, 2023, 321: 122079
30 Zhao W, Jia W, Zhou J, *et al.* Nanoscale grain boundary-weakened Ce–O covalency and surface confinement intrinsically boosting ceria surface oxygen reactivity. J Am Chem Soc, 2025, 147: 13050–13058
31 Wang R, Liu J, Huang Q, *et al.* Partial coordination-perturbed bi-copper sites for selective electroreduction of CO_2 to hydrocarbons. Angew Chem Int Ed, 2021, 60: 19829–19835
32 Li F, Zhao SF, Chen L, *et al.* Polyethylenimine promoted electrocatalytic reduction of CO_2 to CO in aqueous medium by graphene-supported amorphous molybdenum sulphide. Energy Environ Sci, 2016, 9: 216–

© The Author(s) 2026. This article is published with open access at link.springer.com.

223
33 Huang F, Chen X, Sun H, *et al.* Atmosphere induces tunable oxygen vacancies to stabilize single-atom copper in ceria for robust electrocatalytic CO_2 reduction to CH_4. Angew Chem Int Ed, 2025, 64: e202415642
34 Zang Y, Liu T, Wei P, *et al.* Selective CO_2 electroreduction to ethanol over a carbon-coated CuO_x catalyst. Angew Chem, 2022, 134: e202209629
35 Yap FM, Yuan S, Loh JY, *et al. In-situ* probing CO activation in sulfur-enhanced paired electrocatalysis for CO_2-to-C_{2+} conversion with alcohol oxidation. Angew Chem Int Ed, 2025, 64: e202513840
36 Qiao Y, Shen S, Mao C, *et al.* Interfacial oxygen vacancy-copper pair sites on inverse CeO_2/Cu catalyst enable efficient CO_2 electroreduction to ethanol in acid. Angew Chem Int Ed, 2025, 64: e202424248
37 Park S, Jang T, Choi S, *et al.* Iridium-cooperated, symmetry-broken manganese oxide nanocatalyst for water oxidation. J Am Chem Soc, 2023, 145: 26632–26644
38 Ren X, Wang J, Wu H, *et al.* Cu–O geometric coordination induced facet evolution of derived Cu catalysts for efficient CO_2 electroreduction. Sci China Mater, 2025, 68: 3322–3331
39 Wang Z, Li Y, Zhao X, *et al.* Localized alkaline environment via *in situ* electrostatic confinement for enhanced CO_2-to-ethylene conversion in neutral medium. J Am Chem Soc, 2023, 145: 6339–6348
40 Chen Q, Si DH, Wu QJ, *et al.* Engineering copper-based covalent organic framework microenvironments to enable efficient CO_2 electroreduction with tunable ethylene/methane switch. Adv Funct Mater, 2024, 34: 2315368
41 Delmo EP, Wang Y, Song Y, *et al. In situ* infrared spectroscopic evidence of enhanced electrochemical CO_2 reduction and C–C coupling on oxide-derived copper. J Am Chem Soc, 2024, 146: 1935–1945
42 Yang Q, Wang X, Yang Y, *et al.* Electrochemical assembly of a defective Cu catalyst for high current CO_2 electrolysis to methane in a zero-gap electrolyzer. Angew Chem Int Ed, 2025, 64: e202515396
43 Ma F, Zhang P, Zheng X, *et al.* Steering the site distance of atomic Cu–Cu pairs by first-shell halogen coordination boosts CO_2-to-C_2 selectivity. Angew Chem Int Ed, 2024, 63: e202412785

Acknowledgement This work was supported by the Taishan Scholar Program of Shandong Province, China (ts201712045), Shandong Provincial Key Research and Development Program (SPKR&DP) (2019GGX102069), Natural Science Foundation of Shandong Province of China (ZR2018BB008), and Doctoral Fund of Qingdao University of Science and Technology (QUST; 0100229001, 010029081, 010029075).

Funding note Open Access funding enabled and organized by Chung-Ang University.

Author contributions Liu X and Qin Q designed the experiment and supervised its execution. Zhu X synthesized the materials and carried out the electrochemical tests. Zhu X, Zhang Y, Geng Y and Li Z contributed to the characterizations and related discussions. Kim MG and Jang H conducted the XANES measurements. Liu S performed the DFT calculations. Qin Q, Liu X and Zhu X wrote the paper. All the authors discussed the results and commented on the manuscript.

Conflict of interest The authors declare that they have no conflict of interest.

Supplementary information Supplementary materials are available in the online version of the paper.

Open Access This article is licensed under a Creative Commons Attribution 4.0 International License, which permits use, sharing, adaptation, distribution and reproduction in any medium or format, as long as you give appropriate credit to the original author(s) and the source, provide a link to the Creative Commons licence, and indicate if changes were made. The images or other third party material in this article are included in the article's Creative Commons licence, unless indicated otherwise in a credit line to the material. If material is not included in the article's Creative Commons licence and your intended use is not permitted by statutory regulation or exceeds the permitted use, you will need to obtain permission directly from the copyright holder. To view a copy of this licence, visit http://creativecommons.org/licenses/by/4.0/.



Xiaoyue Zhu is currently studying for her Master's degree under the supervision of Prof. Qing Qin and Prof. Xien Liu at Qingdao University of Science and Technology. At present, her research focuses on the preparation and reaction mechanism study of copper-based electro-catalysts for CO_2 reduction.



Qing Qin received her PhD degree from Nankai University in 2017. Now she is a professor of Qingdao University of Science and Technology. Her current research interests focus on the design, synthesis and catalytic mechanism of noble metal- and non-noble metal-based electrocatalysts for electrochemical hydrogen production and CO_2 reduction.



Xien Liu received his PhD degree from Dalian University of Technology. He is currently a professor of Qingdao University of Science and Technology. His research interests focus on the design of electrocatalysts for electrochemical energy conversion and storage devices.

活性位点浓度控制二氧化碳电还原反应路径

朱晓月[1†], 李子健[3†], 张宇航[1], 耿延汝[1], Min Gyu Kim[4], Haeseong Jang[2*], 刘尚果[1*], 刘希恩[1*], 秦清[1*]

摘要 局部活性位点浓度和构型对CO_2还原选择性的关键影响鲜少被探究, 这主要是由于构建明确结构存在挑战. 在本研究中, 我们采用熔盐辅助策略合成了具有可调构型和Cu与Ce-O_V位点相对浓度的Ce-O_V-Cu级联催化剂. 构建了两种不同的几何结构: 一种是密集的铜位点环绕着Ce-O_V, 另一种是孤立的Cu中心被Ce-O_V包裹. 这些构型有效地将关键的*CHO或*COH中间体导向与*CO的耦联或与*H的加氢反应, 从而切换产物选择性. 具有孤立Cu中心的$CuCe_{10}O_x$催化剂在−1.6 V vs. RHE实现了61.7%的高甲烷法拉第效率(FE), 而局部富Cu的$Cu_{10}CeO_x$则有利于C_2的生成, 在−1.4 V vs. RHE时FE_{C_2}为61.5%. 机理研究表明, 局部聚集的Cu位点表现出对*CO_2的强吸附力, 增加了*CO的表面覆盖度, 促进了*CO–*COH耦联; 富含Ce-O_V且具有孤立Cu中心产生丰富的*H, 促进了*CHO中间体向CH_4的深度质子化. 这项工作提出通过调控局域活性中心相对浓度来控制二氧化碳电还原反应路径制备目标产物的新型催化剂设计理念.

© The Author(s) 2026. This article is published with open access at link.springer.com.